

Toward First-Principles Multi-Messenger Predictions: Coupling Nuclear Networks with GR Radiation-MHD in Gmunu

PATRICK CHI-KIT CHEONG (張志杰) ^{1, 2, *} AND CHRISTOPHER L. FRYER ²

¹*Department of Physics, University of California, Berkeley, Berkeley, CA 94720, USA*

²*Center for Nonlinear Studies, Los Alamos National Laboratory, Los Alamos, NM 87545, USA*

ABSTRACT

We present a new implementation of nuclear reaction networks in the General-relativistic multigrid numerical (Gmunu) code, a framework for general relativistic radiation magnetohydrodynamics (GR-RMHD). The extended code self-consistently evolves nuclear species fully coupled to hydrodynamics, magnetic fields, and neutrino radiation transport under the conformal flatness approximation to Einstein’s equations. Four approximate nuclear networks are incorporated, with stiff source terms integrated implicitly using implicit–explicit Runge–Kutta schemes. Validation is performed through a suite of benchmarks, including conserved-to-primitive recovery with a tabulated stellar equation of state, one-zone silicon burning, and hydrodynamic tests of shock tubes, acoustic pulses, and detonation fronts of Type Ia supernovae. These tests confirm accurate coupling between nuclear reactions and fluid dynamics, conserving both electron and nuclear mass fractions to machine precision.

As an application, we perform spherically symmetric core-collapse supernova simulations. The models reproduce the expected non-exploding behavior of standard progenitors, while enhanced neutrino heating leads to shock revival. Including nuclear burning further alters the post-shock composition and dynamics, converting silicon and oxygen layers into iron-group nuclei and strengthening the explosion. This demonstrates the impact of explosive burning on both ejecta composition and shock evolution, and establishes the stability of the coupled GR radiation–MHD–nuclear framework. Although magnetic fields are not evolved in the present 1D application, the implementation is fully compatible with multidimensional GRMHD simulations.

This work represents the first GRRMHD code combining M1 neutrino transport with fully coupled nuclear burning, paving the way for multidimensional studies of supernovae and compact object mergers where nucleosynthesis feedback shapes multi-messenger signals.

1. INTRODUCTION

Nuclear hydrodynamics plays a central role in many astrophysical explosion scenarios, ranging from type Ia supernovae (SNe Ia), classical novae, and X-ray bursts—which are governed by thermonuclear runaway processes—to core-collapse supernovae (CCSNe) and compact object mergers, where nuclear reactions critically influence both the dynamics and observable signals. In these environments, nuclear burning not only powers electromagnetic emission but also drives the synthesis of new elements, thereby shaping the chemical evolution of galaxies. Recent multi-messenger observations, such as gravitational waves from binary neutron

star mergers (Abbott et al. 2017) and high-energy neutrinos and photons from CCSNe, highlight the need for models that consistently incorporate nuclear physics, as these signatures depend sensitively on the interplay of hydrodynamics, neutrino transport, and nucleosynthesis.

Modeling these systems requires a framework that can capture the interplay of strong gravity, neutrino transport, magnetic fields, and nuclear reactions. In particular, CCSNe and neutron star mergers involve conditions extending above and below nuclear saturation density, where relativistic effects and microphysics become equally important. General-relativistic neutrino magnetohydrodynamics (GR ν MHD) codes with coupled nuclear reaction networks are therefore highly desirable for a faithful description of such explosive events.

Significant progress has been made in incorporating reduced nuclear burning into hydrodynamics

patrick.cheong@berkeley.edu

* N3AS Postdoctoral fellow

codes (Nakamura et al. 2014; Couch et al. 2015; Leung et al. 2015; Bruenn et al. 2016; Harris et al. 2017; Wongwathanarat et al. 2017; Sandoval et al. 2021; Bruenn et al. 2020; Navó et al. 2023), though these studies are restricted to Newtonian/special-relativistic frameworks. In parallel, large reaction networks such as `SkyNet` (Lipuner & Roberts 2017) and `WinNet` (Reichert et al. 2023) are often employed in post-processing to calculate detailed nucleosynthesis from tracer particles. While this strategy enables the use of thousands of isotopes, it cannot account for the dynamical feedback of nuclear energy release during the explosion. Fully general-relativistic approaches that self-consistently combine energy-dependent radiation transport, magnetic fields, and nuclear burning remain rare. Some progress has been achieved in general relativity (Montero et al. 2012; Uchida et al. 2017, 2019; Fujibayashi et al. 2025), but most existing implementations rely on highly simplified reaction networks (e.g., CNO cycles) or lack simultaneous support for nuclear equations of state and neutrino transport, thereby constraining their applicability across diverse astrophysical scenarios. The present work therefore represents not only an initial step toward a more comprehensive and physically complete treatment of stellar explosions, but also a bridge between large post-processing networks and reduced in-situ networks within a fully relativistic framework—laying the foundation for future multi-messenger predictions in which nucleosynthesis feedback plays a central role.

In this work, we extend the `Gmunu` code (Cheong et al. 2020, 2021, 2023) by implementing composition evolution, a realistic stellar equation of state, and approximate nuclear networks. Since nuclear burning introduces stiff source terms, we evolve the reactions implicitly. As in our previous work (Cheong et al. 2022, 2023), implicit–explicit (IMEX) Runge–Kutta schemes (see, e.g., Ascher et al. 1997; Pareschi & Russo 2005; Cavaglieri & Bewley 2015) are employed to maintain stability while retaining reasonable step sizes. We validate the implementation through a hierarchy of tests, beginning with the stellar equation of state, followed by one-zone nuclear burning, and culminating in Newtonian verification tests, before demonstrating astrophysical applications in CCSNe.

The paper is organized as follows. Section 2 outlines the methodology and implementation of the stellar equation of state and nuclear networks. Section 3 presents verification tests. Section 4 demonstrates CCSNe simulations with nuclear burning. Finally, Section 5 summarizes our results and discusses future directions.

Unless explicitly stated, we work in geometrized Heaviside-Lorentz units, for which the speed of light c ,

gravitational constant G , solar mass M_\odot , vacuum permittivity ϵ_0 and the Boltzmann constant k_B are all equal to one ($c = G = M_\odot = \epsilon_0 = k_B = 1$). Greek indices, running from 0 to 3, are used for 4-quantities while the Roman indices, running from 1 to 3, are used for 3-quantities.

2. METHODS

2.1. Formulations

`Gmunu` adopts the 3 + 1 reference-metric formalism (Montero et al. 2014; Mewes et al. 2020; Baumgarte & Shapiro 2020). In this formalism, the metric can be written as

$$ds^2 = g_{\mu\nu} dx^\mu dx^\nu = -\alpha^2 dt^2 + \gamma_{ij} (dx^i + \beta^i dt) (dx^j + \beta^j dt), \quad (1)$$

where α is the lapse function, β^i is the spacelike shift vector, and γ_{ij} is the spatial metric. We adopt a conformal decomposition of the spatial metric γ_{ij} with the conformal factor ψ :

$$\gamma_{ij} = \psi^4 \bar{\gamma}_{ij}, \quad (2)$$

where $\bar{\gamma}_{ij}$ is the conformally related metric. This conformally related metric can be expressed as the sum of a background *time-independent* reference metric $\hat{\gamma}_{ij}$ and deviations h_{ij}^{dev} . In our current implementation, the reference metric $\hat{\gamma}_{ij}$ is the flat spacetime metric of the chosen coordinate system (i.e., either Cartesian, cylindrical, or spherical coordinates). Note that, in conformally flat approximations, the spacetime deviations vanish and the reference metric is the conformally related metric (i.e., $\bar{\gamma}_{ij} = \hat{\gamma}_{ij}$).

`Gmunu` solves the general relativistic radiation magnetohydrodynamics. The evolution equations for the system are derived from the local conservation of rest-mass and energy-momentum, and from the homogeneous Faraday’s law. Moreover, depending on applications, evolution of the electron fraction and neutrino number densities are also available. Details of the implementation of these equations are documented in (Cheong et al. 2020, 2021, 2022, 2023, 2024). Below, we focus on the additional equations for nuclear hydrodynamics.

The evolution of the mass fraction of the l -th species X_l is given by (Fujibayashi et al. 2025):

$$\frac{1}{\sqrt{-g}} \partial_\mu (\sqrt{-g} \rho X_l u^\mu) = A_l m_u \dot{n}_{\text{nuc}}, \quad (3)$$

where g is the determinant of the spacetime metric, ρ is the rest-mass density of the fluid, u^μ is the fluid four-velocity, and m_u is the atomic mass unit. A_l and \dot{n}_{nuc}

are the mass number and the change rate of the l -th species, respectively.

As in our previous work (e.g., [Cheong et al. \(2021\)](#)), the evolution equations of the mass fraction (3) can be expressed in the form:

$$\partial_t \mathbf{q} + \frac{1}{\sqrt{\hat{\gamma}}} \partial_j \left[\sqrt{\hat{\gamma}} \mathbf{f}^j \right] = \mathbf{s}. \quad (4)$$

Here,

$$q_{DX_l} \equiv \sqrt{\gamma/\hat{\gamma}} [\rho X_l W], \quad (5)$$

$$(f_{DX_l})^i \equiv \sqrt{\gamma/\hat{\gamma}} [\rho X_l W \hat{v}^i], \quad (6)$$

$$s_{DX_l} \equiv \sqrt{\gamma/\hat{\gamma}} [\alpha A_l m_u \dot{n}_{\text{nuc}}], \quad (7)$$

where $\hat{v}^i \equiv (\alpha v^i - \beta^i)$, v^i is the three-velocity measured by an Eulerian observer at rest in the current spatial 3-hypersurface, and $W \equiv 1/\sqrt{1 - v^i v_i}$ is the Lorentz factor.

2.2. Equations of State

Equations of state (EoSs) that depend on isotopic composition are necessary for nuclear hydrodynamical simulations. In this work, the Helmholtz-type stellar EoS is provided by coupling to the EoS driver `helmeos` ([Timmes & Swesty 2000](#)). In this EoS, the fluid is composed of ideal gas ions, radiation, and degenerate or relativistic electrons, in local thermodynamic equilibrium. Additionally, we include the average mass excess per baryon contribution to the internal energy density:

$$\epsilon = \epsilon_{\text{th}}(\rho, T, \{X_l\}) + \frac{1}{m_u} \sum_l \Delta m_l Y_l, \quad (8)$$

where $\epsilon_{\text{th}}(\rho, T, \{X_l\})$ is the thermal energy density provided by `helmeos`, $Y_l = X_l/A_l$ is the molar abundance, and

$$\Delta m_l = m_l - A_l m_u \quad (9)$$

is the mass excess of the l -th species with atomic mass m_l . This formulation allows the internal energy to remain unchanged during nuclear reactions, with the thermal energy adjusting accordingly when the composition changes ([Perego et al. 2015](#); [Hasenour & Duffell 2025](#)).

As noted in [O'Connor & Ott \(2010\)](#), the zero point for the specific internal energy ϵ is not arbitrary, as it affects the energy-momentum tensor and, thus, spacetime evolution. Rest-mass contributions must not be included in ϵ , and the reference rest mass in the EoS must be consistent across regimes.

Gmunu adopts the conserved-to-primitive conversion scheme of [Kastaun et al. \(2021\)](#), where the minimum specific enthalpy is required. With the specific energy given by (8), the minimum specific enthalpy is estimated as $h_{\text{min}} \approx \min(m_l/A_l/m_u)$.

2.2.1. Transition to Nuclear Statistical Equilibrium region

As most of our targeted systems involve neutron stars, a nuclear EoS that handles matter at high density (e.g. $\rho \gtrsim 10^8 \text{ g} \cdot \text{cm}^{-3}$) is needed. Currently, **Gmunu** adopts tabulated nuclear EoSs assuming nuclear statistical equilibrium (NSE) between protons, neutrons, alpha particles, and a representative heavy nucleus for these regions.

Connecting the nuclear and stellar EoSs smoothly is desired for applications that involve both high and low density regions. The implementation of the transition between these regions is problem dependent. For example, various approaches have been proposed in the context of core-collapse supernovae ([Rampp & Janka 2002](#); [Buras et al. 2006](#); [Perego et al. 2015](#); [Bruenn et al. 2020](#); [Navó et al. 2023](#)).

Here, we adopt an approach similar to the one reported in [Perego et al. \(2015\)](#); [Navó et al. \(2023\)](#). Specifically, in regions where the rest-mass density is covered by both nuclear and stellar EoSs, we choose the temperature thresholds $T_{\text{hi}} = 5.8 \text{ GK}$ and $T_{\text{lo}} = 5 \text{ GK}$. Nuclear EoS is used when $T \geq T_{\text{hi}}$, while stellar EoS is used when $T < T_{\text{lo}}$. In the mixed region $T_{\text{lo}} \leq T < T_{\text{hi}}$, thermodynamical quantities are obtained via linear interpolation between the two EoSs. Finally, when the density is outside the nuclear EoS table, the stellar EoS is used, and vice versa.

In the nuclear EoS region (i.e. $T \geq T_{\text{hi}}$), only Y_e is required and X_l is not needed. In the stellar EoS region (i.e. $T < T_{\text{lo}}$), the mass fractions X_l are needed, and the electron fraction is overwritten as $Y_e = \sum_l X_l Z_l/A_l$. In the mixed region, both Y_e and X_l must be consistent. Here, we assume NSE compositions, where X_l is given by an NSE solver (see Section 2.3.2). To minimize calls to the NSE solver, we evolve both Y_e and X_l throughout the domain, monitoring the difference between the advected Y_e and $Y_e(\{X_l\})$ in the mixed region. If the absolute difference exceeds 10^{-3} , the NSE solver overwrites X_l .

Usually, despite different physics considered in nuclear and stellar EoSs, the physical properties at densities $\rho \sim 10^7 - 10^8 \text{ g} \cdot \text{cm}^{-3}$ are similar ([Rampp & Janka 2002](#)). The EoSs start to differ at $\rho \gtrsim 10^7 \text{ g} \cdot \text{cm}^{-3}$. Moreover, the specific energy ϵ in the nuclear EoS is usually insensitive to temperature when $T \lesssim 1 \text{ MeV} \approx 11.6 \text{ GK}$. Therefore, when solving for T given ϵ , a solution may exist in both EoSs for $\rho \gtrsim 10^7 \text{ g} \cdot \text{cm}^{-3}$ and $T \lesssim 10^{10} \text{ K}$. In the context of CCSNe, the temperature in high-density regions is usually high enough to assume NSE ([Rampp & Janka 2002](#); [Navó et al. 2023](#)). In this work, we prioritize the solution available in the nuclear EoS, using the stellar EoS only when necessary. We remind the reader

that the implementation of EoS bridging is problem dependent; careful choice of EoSs and bridging methods is required.

2.3. Nuclear Network

Several approximate nuclear networks are implemented in `Gmnu`. Specifically, 7-, 13-, 19-, and 21-species networks are available via `iso7`, `aprox13`, `aprox19`, and `aprox21` (Timmes 1999; Timmes et al. 2000). Here, we focus on the standard 13-species α -chain network: ${}^4\text{He}$, ${}^{12}\text{C}$, ${}^{16}\text{O}$, ${}^{20}\text{Ne}$, ${}^{24}\text{Mg}$, ${}^{28}\text{Si}$, ${}^{32}\text{S}$, ${}^{36}\text{Ar}$, ${}^{40}\text{Ca}$, ${}^{44}\text{Ti}$, ${}^{48}\text{Cr}$, ${}^{52}\text{Fe}$, ${}^{56}\text{Ni}$.

2.3.1. Coupling to Hydrodynamics

The timescale of the change rate of certain isotopes in the source term (7) can be comparable to or even shorter than the hydrodynamical timescale. In such cases, the reaction-induced source terms can be very stiff from a numerical point of view. Applying explicit time integration would be inefficient due to extremely strict constraints on the time step, potentially requiring prohibitively small steps to maintain stability. Therefore, nuclear reactions are often treated implicitly, for example using operator splitting (most notably Strang (Strang 1968)) (Hasenour & Duffell 2025), first-order implicit Euler schemes (Lippuner & Roberts 2017; Navó et al. 2023), or higher-order methods based on spectral deferred correction (Zingale et al. 2019).

In this work, we adopt implicit-explicit (IMEX) Runge-Kutta schemes (Ascher et al. 1997; Pareschi & Russo 2005), which have been applied and tested previously in `Gmnu` for resistive magnetohydrodynamics (Cheong et al. 2022) and radiation transfer (Cheong et al. 2023). The key advantage of IMEX schemes is that they allow the stiff source terms from nuclear reactions to be treated implicitly, while the non-stiff hydrodynamical fluxes are handled explicitly. This approach provides stability for stiff reactions without sacrificing efficiency in the advection-dominated hydrodynamics. For implementation details of IMEX in `Gmnu`, we refer readers to Cheong et al. (2022).

An implicit update of the mass fraction $\{X_l\}$ from timestep \mathbf{n} (denoted $\mathbf{q}^{\mathbf{n}}$) to $\mathbf{n}+1$ (denoted $\mathbf{q}^{\mathbf{n}+1}$) can be expressed as

$$\mathbf{q}^{\mathbf{n}+1} = \mathbf{q}^{\mathbf{n}} + \Delta t \mathbf{s}_{\text{stiff}}(\mathbf{q}^{\mathbf{n}+1}), \quad (10)$$

where $\mathbf{s}_{\text{stiff}}$ represents the stiff source terms, given by equation (7) in this case. To obtain $\mathbf{q}^{\mathbf{n}+1}$, we solve the non-linear system

$$\mathbf{f}(\mathbf{q}) \equiv -\mathbf{q} + \mathbf{q}^{\mathbf{n}} + \Delta t \mathbf{s}_{\text{stiff}}(\mathbf{q}). \quad (11)$$

During the implicit step, we assume that the spacetime metric and all primitive variables (e.g., ρ , v^i , T) remain

unchanged except for the mass fractions $\{X_l\}$. Thus, the source term can be expressed as

$$s_{DX_l} = \sqrt{\gamma/\tilde{\gamma}} \left[\alpha \rho \dot{X}_l \right], \quad (12)$$

where $\{\dot{X}_l\}$ are provided by the nuclear network modules.

Traditionally, nuclear reactions are treated as sets of first-order ordinary differential equations (ODEs) and solved with standard ODE integrators (Mueller 1986; Hix & Thielemann 1999; Timmes 1999; Hasenour & Duffell 2025). Here, we solve the non-linear system using a multidimensional Broyden method, falling back to the Newton-Raphson method if the Broyden method fails. The Jacobian $\partial f_i / \partial q_j$ is computed analytically, with derivatives of the mass fraction change rates provided by the nuclear network modules. The implementation of the Broyden solver and Jacobian computation follows Press et al. (1996).

It is worth noting that the neutrino transfer module in `Gmnu` shares the same IMEX infrastructure as nuclear burning. However, in the current implementation, they operate in different density and temperature regimes, allowing both modules to be used simultaneously without conflict.

Shocks are typically under-resolved in astrophysical simulations due to the finite numerical resolution. To mitigate spurious results, it is common to suppress nuclear burning inside numerical shocks (Fryxell et al. 1989), ensuring that burning only occurs once physically appropriate post-shock conditions are established. In our implementation, we adopt a simplified version of the approach described in Zingale et al. (2024); Brady & Zingale (2025), tagging a cell as shocked when

$$\frac{|\nabla P \cdot \vec{v}|}{P |v|} > f_{\text{shock}}, \quad (13)$$

$$\nabla \cdot \vec{v} < 0,$$

where $f_{\text{shock}} = 2/3$ by default. Here, ∇P and $\nabla \cdot \vec{v}$ are computed using slope-limited reconstructions (e.g., TVD or PPM limiters) to suppress oscillations near discontinuities and return a monotonic, cell-centred slope. This criterion effectively identifies cells with significant pressure jumps along the flow direction that are also undergoing compression, marking them as part of the shock region. Although we have not conducted an extensive parameter study ourselves, previous investigations indicate that variations of f_{shock} within the range 0.5–1.0 do not qualitatively alter the dynamics (Brady & Zingale 2025). Alternative formulations, such as normalizing the pressure gradient by the local grid spacing rather than projecting along the velocity, have been shown to perform equivalently (Gronow et al. 2020).

For all cells flagged as shocked, nuclear burning is temporarily disabled to prevent unphysical energy generation. While this approach is simple, it provides a robust and computationally efficient method for shock treatment in nuclear hydrodynamics. Future work will include implementing a dedicated test to explicitly verify the impact of this prescription and exploring refinements such as adaptive shock-capturing schemes or burning suppression based on additional physical criteria.

2.3.2. NSE solver

An NSE solver that computes isotope compositions under NSE for a given thermodynamic state is often required for consistent composition evolution. For regions that reach NSE, applying a nuclear network is unnecessary: compositions there can be set to satisfy NSE conditions. The NSE solver can also be used to initialize compositions at the start of a simulation. Our implementation of the NSE solver closely follows the methods described in [Calder et al. \(2007\)](#); [Seitenzahl et al. \(2009, 2008\)](#). Below, we outline the implementation details.

The mass fractions in NSE are obtained by solving

$$\begin{aligned} \sum_l X_l (\mu_p^{\text{kin}}, \mu_n^{\text{kin}}) &= 1, \\ \sum_l \frac{Z_l}{A_l} X_l (\mu_p^{\text{kin}}, \mu_n^{\text{kin}}) &= Y_e, \end{aligned} \quad (14)$$

numerically for the chemical potentials of the kinetic part of the free protons and neutrons μ_p^{kin} and μ_n^{kin} . Each mass fraction is

$$\begin{aligned} X_l (\mu_p^{\text{kin}}, \mu_n^{\text{kin}}) &= \frac{m_l}{\rho} g_l \left(\frac{2\pi m_l k_B T}{h^2} \right)^{3/2} \\ &\times \exp \left(\frac{Z_l \mu_p^{\text{kin}} + N_l \mu_n^{\text{kin}} + Q_l - \mu_l^C + Z_l \mu_p^C}{k_B T} \right), \end{aligned} \quad (15)$$

with $N_l = A_l - Z_l$, Q_l the nuclear binding energy, h Planck's constant, k_B Boltzmann's constant. g_l is the nuclear partition functions of nucleus l , which is in general temperature dependent. Nevertheless, in this work, we simply set $g_l = 2$, and the inclusion of tabulating more realistic tables (e.g. [Rauscher & Thielemann \(2000\)](#)) is left as future work. μ_l^C is the Coulomb corrections, which is obtained by using the fitting form by [Chabrier & Potekhin \(1998\)](#):

$$\begin{aligned} \frac{\mu_l^C}{k_B T} &= A_1 \left[\sqrt{\Gamma_l (A_2 + \Gamma_l)} - A_2 \ln \left(\sqrt{\frac{\Gamma_l}{A_2}} + \sqrt{1 + \frac{\Gamma_l}{A_2}} \right) \right] \\ &+ 2A_3 \left[\sqrt{\Gamma_l} - \arctan \left(\sqrt{\Gamma_l} \right) \right], \end{aligned} \quad (16)$$

where $A_1 = -0.9052$, $A_2 = 0.6322$, and $A_3 = -\sqrt{3}/2 - A_1/\sqrt{A_2}$. $\Gamma_l = Z_l^{5/3} \Gamma_e$ is the ion-specific Coulomb

coupling parameter with $\Gamma_e = e^2 (4\pi n_e/3)^{1/3} / (k_B T)$, where the electron number density is estimated as $n_e = Y_e \rho / m_u$.

The constrained system (14) is solved numerically using the Newton-Raphson method.

3. CODE TESTS

Although our ultimate goal is to apply nuclear burning in general-relativistic simulations, it is essential to benchmark the EoS and nuclear-reaction modules individually. Comparisons with well-established Newtonian test problems provide robust validation of the implementation. In this section we first test the modules and the code in the Newtonian regime, then present general-relativistic examples in Section 4.

3.1. Specific energy to temperature inversion

The specific energy ϵ is required for hydrodynamical evolutions, while the EoSs typically use temperature T as an input rather than ϵ . Calculating the specific energy from a given temperature (i.e., $\epsilon(T)$) is straightforward. However, inverting from specific energy to temperature (i.e., $T(\epsilon)$) is non-trivial and often requires a root-finding procedure.

Here, we test our implementation of the specific energy-to-temperature inverter. The workflow of the round-trip test is

$$T \xrightarrow{\text{EoS}} \epsilon \xrightarrow{\epsilon\text{-}T \text{ root finding}} T' \xrightarrow{\text{EoS}} \epsilon'. \quad (17)$$

The relative error of T is then calculated as

$$\text{relative error of } T = \left| \frac{T'}{T} - 1 \right|, \quad (18)$$

with a similar definition for the relative error of ϵ .

We sample the rest-mass density and temperature over $-10 \leq \log_{10}(\rho [\text{g} \cdot \text{cm}^{-3}]) \leq 15$ and $4 \leq \log_{10}(T [\text{K}]) \leq 12$, using 32 points in each direction. The electron fraction Y_e is set to $\{0.5, 0.4, 0.3, 0.2, 0.1\}$. The SFHo EoS ([Steiner et al. 2013](#)) is used for the NSE region. For non-NSE regions, mass fractions $\{X_l\}$ are required. Instead of assuming NSE everywhere, we assign $\{X_l\}$ based on a ‘‘two-species mixture’’ for a given Y_e . Specifically, we scan from the lightest to heaviest isotopes and identify two isotopes i and j such that $Z_i/A_i \leq Y_e \leq Z_j/A_j$. The mass fractions are then assigned as

$$X_i = \frac{Y_e - Z_j/A_j}{Z_i/A_i - Z_j/A_j}, \quad X_j = 1 - X_i. \quad (19)$$

Figure 1 shows the relative errors of temperature T and specific energy ϵ for the round-trip tests with different electron fractions Y_e . As discussed in Section 2.2.1,

the solution T of $\epsilon = \epsilon(T)$ may exist in both EoSs in regions where $\rho \gtrsim 10^7 \text{ g} \cdot \text{cm}^{-3}$ and $T \lesssim 10^{10} \text{ K}$. Since the code prioritizes the solution available in the nuclear EoS, the temperature is not exactly recovered in these regions, which corresponds to the white areas in the lower-right part of the figures. Nevertheless, the relative error of the specific energy in these regions remains below 10^{-14} (bottom panels). Therefore, as long as no microphysics explicitly requires the temperature in these regions, the hydrodynamical evolution is expected to remain accurate.

3.2. Conserved-to-primitive conversion

Recovery of primitive variables from conservative variables in GRMHD is a non-trivial process, requiring the numerical solution of non-linear equations. As discussed in Section 2.2, `Gmnu` adopts the conserved-to-primitive conversion scheme of Kastaun et al. (2021). Although this scheme has been successfully applied with tabulated nuclear EoSs, it warrants re-testing due to the special bridging between stellar and nuclear EoSs.

The primitive vector is defined as

$$\mathbf{p} = [\rho, Wv^i, \log(T), B^i, Y_e, X_l]. \quad (20)$$

To assess the solver performance, we sample the primitive variables over a specified range, compute the corresponding conservative variables, then recover the primitive variables and compare them to the original vector. The accuracy is quantified via (Siegel et al. 2018)

$$\text{error} = \frac{1}{N_p} \sum_{i=1}^{N_p} \left| \frac{\mathbf{p}_i - \mathbf{p}'_i}{\mathbf{p}'_i} \right|, \quad (21)$$

where N_p is the number of primitive variables.

While the primitive vector often uses the specific energy ϵ rather than temperature T (e.g., Siegel et al. (2018)), we measure the error using T because it is required for many microphysics calculations, such as nuclear burning and neutrino transport. Consequently, relative errors with T are generally larger than those with ϵ (see Figure 1).

Figure 2 shows the averaged error in conserved-to-primitive conversions, sampling ρ and T for selected Lorentz factors W , electron fractions Y_e , and magnetization $\beta_{\text{mag}} = P_{\text{gas}}/P_{\text{mag}} = 1000$ (weakly magnetized case). White regions in the lower right reflect temperature recovery issues discussed in Section 3.1. The upper-left region (low density, high temperature) exhibits larger errors for higher Lorentz factors because, in this regime, kinetic energy dominates the conserved variables, making the solution insensitive to thermal energy and causing precision loss due to floating-point cancellation. Tests with stronger magnetic fields (down to

$\beta_{\text{mag}} = 10^{-3}$) show similar behavior and are not shown. Overall, the majority of the parameter space exhibits relative errors below 10^{-8} , with errors near the edges reaching $\lesssim 10^{-4}$.

3.3. Pure Silicon Burning Test

To verify that the nuclear burning module drives compositions consistently toward NSE, we performed a one-zone calculation starting from pure ^{28}Si . This setup has long been used as a benchmark in nuclear network studies (e.g., Woosley et al. (1973); Hix & Thielemann (1996, 1999); Timmes et al. (2000)), since silicon burning rapidly produces an iron-group dominated composition under high temperatures and densities.

We fix the thermodynamic conditions at $\rho = 10^7 \text{ g} \cdot \text{cm}^{-3}$ and $T = 6 \text{ GK}$, and evolve the composition using our nuclear reaction network. The evolution is performed over a time domain sampled uniformly in \log_{10} space from 10^{-12} to 1 s with 1000 points, which directly sets the integration timesteps. Thanks to the robustness of the Netwon-Raphson solver, the test proceeds smoothly even under this aggressive timestep choice. Weak interactions are neglected, and therefore the electron fraction Y_e remains constant throughout the calculation. The system evolves until the net reaction flows approach detailed balance, indicating relaxation to nuclear statistical equilibrium (Figure 3).

To ensure the numerical integrity of the network, we monitor conservation properties:

- **Mass fraction sum:** $\sum_l X_l$ should remain unity, as the network only redistributes composition without creating or destroying total nucleon number.
- **Electron fraction:** Y_e must remain constant in the absence of weak interactions, providing an independent check of numerical consistency.

The final abundances are compared with predictions from the NSE solver at the same thermodynamic state. The network converges toward the expected equilibrium distribution. The integrated energy release during burning matches the binding energy differences implied by the evolving composition, confirming the correct coupling of the network to the equation of state.

The NSE abundances and the asymptotic abundances from the network calculation show slight differences. This arises because the Coulomb physics treated in the NSE solver and in the `aprox13` network are not identical. The NSE module incorporates Coulomb corrections following Chabrier & Potekhin (1998). In contrast, `aprox13` accounts for Coulomb effects through screen-

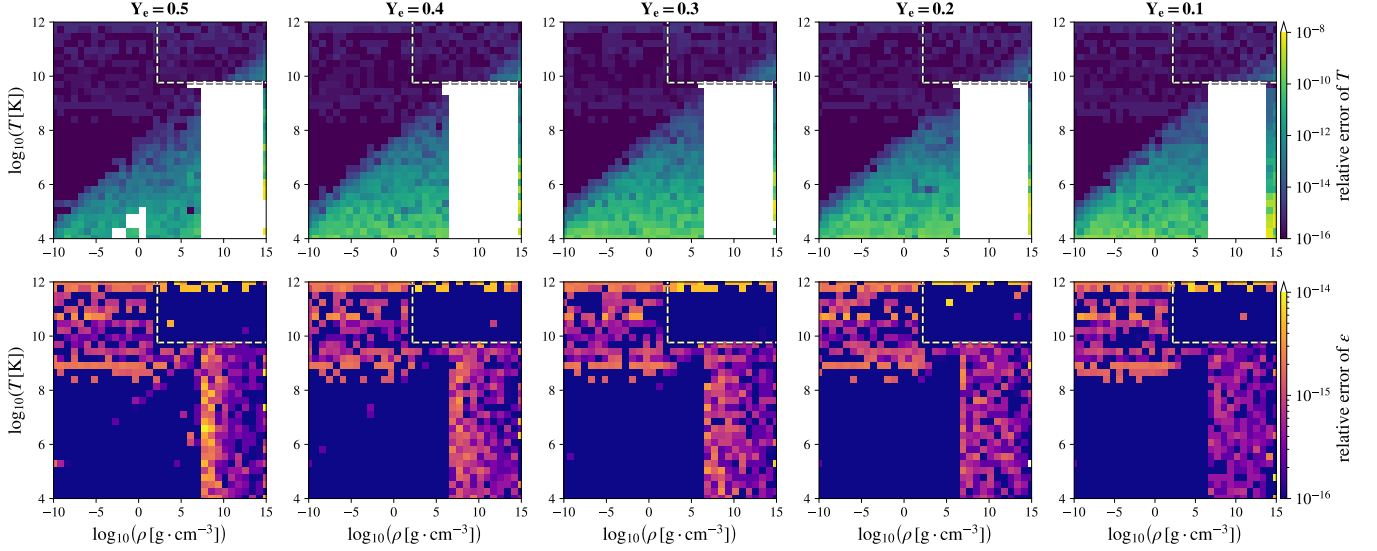


Figure 1. Relative errors of temperature T (top) and specific energy ϵ (bottom) from the round-trip tests for five electron fractions Y_e . The upper-right regions enclosed by the white dashed lines denote where the nuclear EoS is applied, while the stellar or transitional (mixed) EoS is used elsewhere. The mixed regime corresponds to $5 < T < 5.8$ GK where both the stellar and nuclear EoS tables overlap in density. At densities $\rho \gtrsim 10^7 \text{ g cm}^{-3}$ and temperatures $T \lesssim 10^{10}$ K, the temperature recovery is imperfect because the code prioritizes solutions from the nuclear EoS (see Section 2.2.1). Nevertheless, the relative error in the specific energy ϵ , which serves as a primitive variable in hydrodynamical evolution, remains below 10^{-14} across the explored parameter space.

ing corrections to reaction rates based on Wallace et al. (1982).

This test demonstrates that the network reliably drives material from a non-equilibrium initial composition to NSE under fixed conditions, establishing a controlled baseline for subsequent tests that include hydrodynamic and relativistic coupling. In particular, conservation of $\sum X_i$ and Y_e in this simple setup builds confidence that these quantities will remain robust when the network is coupled to full multidimensional simulations, where violations could otherwise accumulate and compromise the long-term stability of the calculation.

3.4. Newtonian Real Gas Shock Tubes

To verify the stellar EoS implementation, we perform the Newtonian real gas shock tube test introduced by Zingale & Katz (2015), for which exact solutions are available. The simulations are carried out in Cartesian coordinates.

Following test 1 of Zingale & Katz (2015), the initial conditions are

$$(\rho, T, v) = \begin{cases} (\rho_L, T_L, v_L), & \text{if } x < 0.5L, \\ (\rho_R, T_R, v_R), & \text{if } x > 0.5L, \end{cases} \quad (22)$$

with parameters

$$\rho_L = 10^7 \text{ g} \cdot \text{cm}^{-3}, \quad \rho_R = 10^6 \text{ g} \cdot \text{cm}^{-3}, \quad (23)$$

$$T_L = 10^8 \text{ K}, \quad T_R = 10^6 \text{ K}, \quad (24)$$

$$v_L = 0, \quad v_R = 0, \quad (25)$$

and domain length $L = 10^6$ cm. The composition is set to pure ^{12}C .

Figure 4 shows the profiles of rest-mass density ρ , velocity v , pressure P , and temperature T at $t = 8 \times 10^{-4}$ s. The numerical results from *Gmunu* (red dots) agree well with the reference exact solutions (black solid lines), confirming the correct implementation of the stellar EoS in Newtonian regimes.

3.5. Newtonian Real Gas Acoustic Pulse in 1D

Smooth tests are ideal for assessing the convergence of the implementation. Here, we perform the Newtonian real gas acoustic pulse test introduced in Zingale et al. (2019) to validate both hydrodynamics and nuclear burning in *Gmunu*. The initial pressure and specific entropy profiles are prescribed as:

$$p(x) = p_0 \left[1 + f_p \exp\left(-\frac{x^2}{\delta_r^2}\right) \cos^6\left(\frac{\pi x}{L_x}\right) \right], \quad (26)$$

$$s(x) = s_0, \quad (27)$$

where f_p and δ_r set the amplitude and width of the perturbation, L_x is the domain size in the x -direction, and

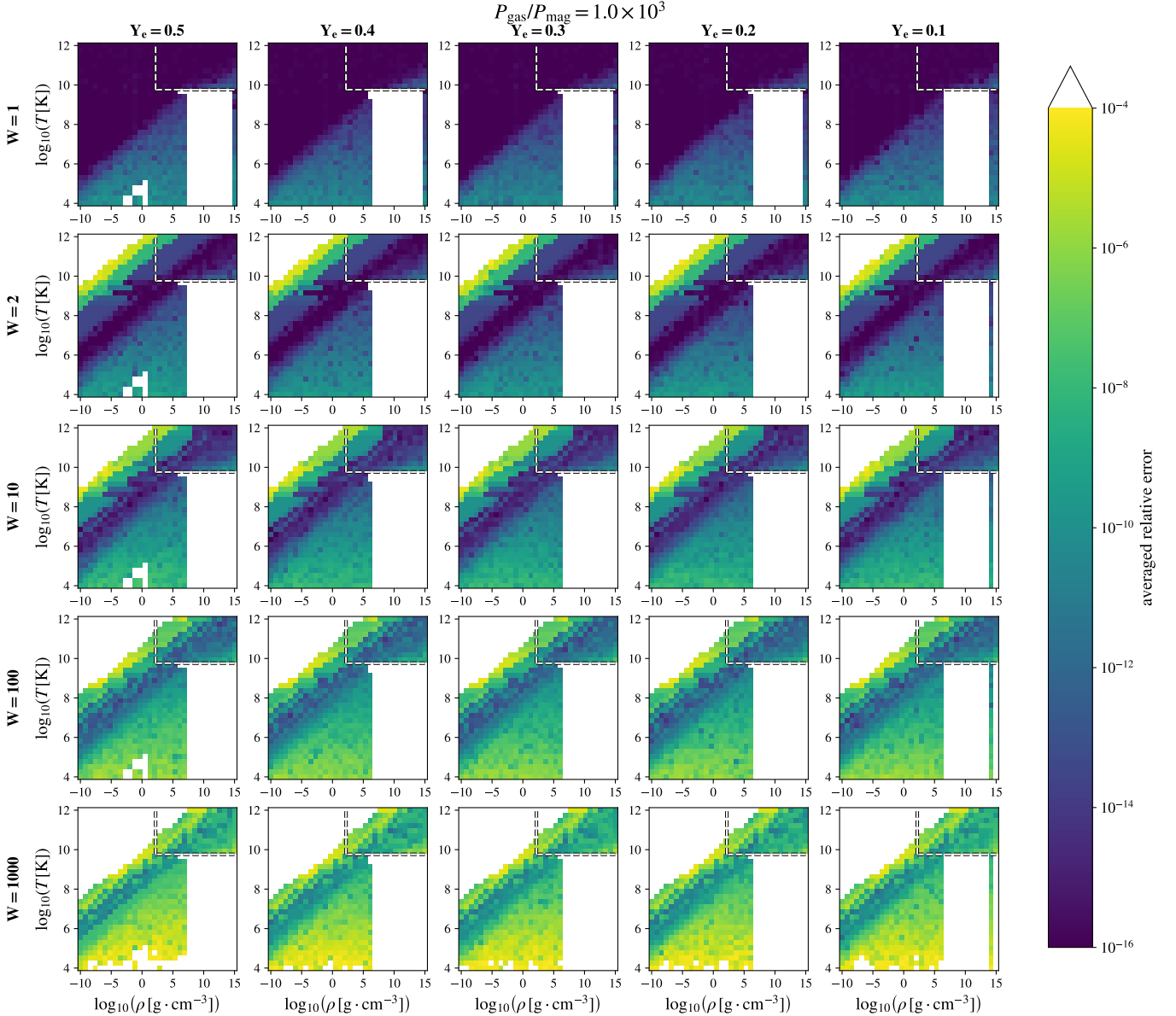


Figure 2. Averaged relative error in conserved-to-primitive tests for selected Lorentz factors W , electron fractions Y_e , and magnetization $\beta_{\text{mag}} = 1000$ (weakly magnetized case). The upper-right regions enclosed by the white dashed lines denote where the nuclear EoS is applied, while the stellar or transitional (mixed) EoS is used elsewhere.

x is the spatial coordinate. The ambient pressure p_0 and specific entropy s_0 are determined from the background density ρ_0 and temperature T_0 , i.e., $p_0 = p(\rho_0, T_0)$ and $s_0 = s(\rho_0, T_0)$.

Following [Hasenour & Duffell \(2025\)](#), we adopt $\rho_0 = 5 \times 10^5 \text{ g} \cdot \text{cm}^{-3}$, $T_0 = 3 \times 10^8 \text{ K}$, $f_p = 2$, $\delta_r = 2 \times 10^7 \text{ cm}$, and $L_x = 10^8 \text{ cm}$. The fluid is initially composed of pure ${}^4\text{He}$.

We employ the 2nd-order accurate strong-stability preserving IMEX-SSP2(2,2,2) time integrator ([Pareschi & Russo 2005](#)), the Harten-Lax-van Leer (HLL) Riemann solver, and a 2nd-order monotized central (MC)

limiter ([van Leer 1974](#)). For the nuclear-reacting cases, the 13-species network `aprox13` is coupled to the hydrodynamics.

Figure 5 shows snapshots of the rest-mass density ρ at six times for $N = 128$ grid points. The comparison between purely hydrodynamical evolution (upper panel) and the nuclear-reacting case (lower panel) demonstrates that nuclear burning significantly affects the expansion dynamics of the fluid.

To quantify convergence, we perform simulations at multiple spatial resolutions and compute the volume-weighted L_1 norm of the rest-mass density relative to a

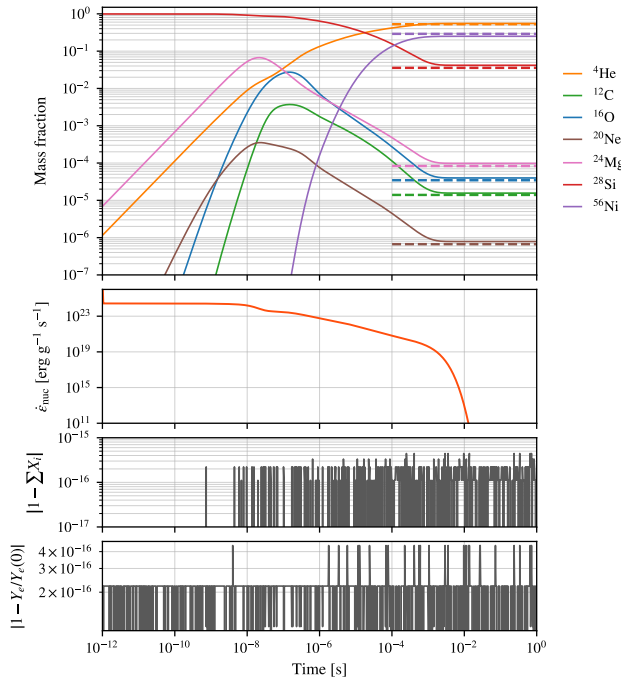


Figure 3. One-zone pure silicon burning test at fixed $\rho = 10^7 \text{ g} \cdot \text{cm}^{-3}$ and $T = 6 \times 10^9 \text{ K}$, starting from pure ^{28}Si . The network evolves the composition toward an iron-group dominated state consistent with nuclear statistical equilibrium. *Top panel:* Mass fractions of selected species (solid) and NSE predictions (dashed). *Middle panel:* Energy generation rate. *Bottom panels:* Deviations from conservation: $|1 - \sum X_i|$ and $|1 - Y_e/Y_e(0)|$.

high-resolution reference solution ($N_{\text{ref}} = 2048$):

$$L_1(N) = \frac{\sum_{i=1}^N \Delta x[i] \times |\rho[i] - \rho_{\text{ref}} [\frac{N_{\text{ref}}}{N} \times i]|}{\sum_{i=1}^N \Delta x[i]}, \quad (28)$$

where $\Delta x[i]$ is the local cell width and i indexes the grid points. The diagnostic is evaluated at $t_f = 0.02 \text{ s}$. A fixed timestep scaled with resolution is adopted following Zingale et al. (2019):

$$\Delta t = 2 \times 10^{-4} \left(\frac{64}{N} \right) \text{ s}. \quad (29)$$

As discussed by Hasenour & Duffell (2025), entropy is not conserved when nuclear burning is active; therefore, we monitor convergence using the rest-mass density instead.

Figure 6 shows L_1 as a function of resolution N . Second-order convergence is observed, in agreement with the 2nd-order time integrator and spatial reconstruction.

3.6. Detonation front of SNe Ia in 1D

To validate our burning limiter prescription, we reproduce a test problem originally proposed by Papatheodore & Messer (2014), which examines detonations

in the outer reactive layers of Type Ia supernovae. This test provides a clean setup for studying the coupling between hydrodynamic shocks and nuclear burning.

The 2nd-order accurate strong-stability preserving IMEX-SSP2(2,2,2) time integrator (Pareschi & Russo 2005), the Harten-Lax-van Leer (HLL) Riemann solver, and a 2nd-order monotized central (MC) limiter (van Leer 1974), are employed in this test. The computational domain spans $[0, 4096] \text{ cm}$ and is discretized with 256 base zones, allowing up to six levels of adaptive mesh refinement (AMR) that track the burning fronts of the ^{12}C and ^{16}O mass fractions. At the highest refinement level, the effective grid spacing is $\Delta x = 0.5 \text{ cm}$. Reflective boundary conditions are applied at the left boundary (ash side), while outflow boundary conditions are imposed at the right boundary (fuel side). The unperturbed region initially has a uniform rest-mass density and temperature of $\rho = \rho_0$ and $T = 10^7 \text{ K}$, respectively, with equal mass fractions of ^{12}C and ^{16}O only. We consider four density setups with $\rho_0 = 5 \times 10^7, 1 \times 10^8, 5 \times 10^8, \text{ and } 1 \times 10^9 \text{ g} \cdot \text{cm}^{-3}$. To initiate the detonation, we set $T = 10^{10} \text{ K}$ and $v^x = 10^9 \text{ cm} \cdot \text{s}^{-1}$ for $x < 25 \text{ cm}$.

We perform simulations both with and without the burning limiter mechanism described in Section 2.3.1. In the runs with suppression enabled, nuclear burning is deactivated in zones flagged as shocked, thereby preventing premature or spurious nuclear energy release at the shock front.

Figure 7 shows the rest-mass density profiles at $t = 10^{-6} \text{ s}$ for models with and without burning suppression. Solid lines denote cases where burning is prohibited in shocked regions, while dashed lines correspond to runs where burning is always allowed. Overall, our results qualitatively reproduce the trends reported by Papatheodore & Messer (2014): cases without suppression develop slightly faster-moving shocks due to additional energy deposition from unphysical burning immediately behind the shock. The absolute shock locations differ marginally from those in their study, likely due to differences in the precise output time (their figure does not show results exactly at $t = 10^{-6} \text{ s}$) and in the numerical schemes used.

However, we do not observe the secondary shock structure reported by Papatheodore & Messer (2014). This discrepancy may stem from our use of an IMEX time-integration scheme with direct Newton–Raphson coupling between hydrodynamics and nuclear burning, whereas most previous nuclear hydrodynamics codes evolve the reaction network via operator-split ODE solvers. In addition, differences in numerical dissipation—arising from less diffusive Riemann solvers, reconstruction methods, or the AMR configuration—may also

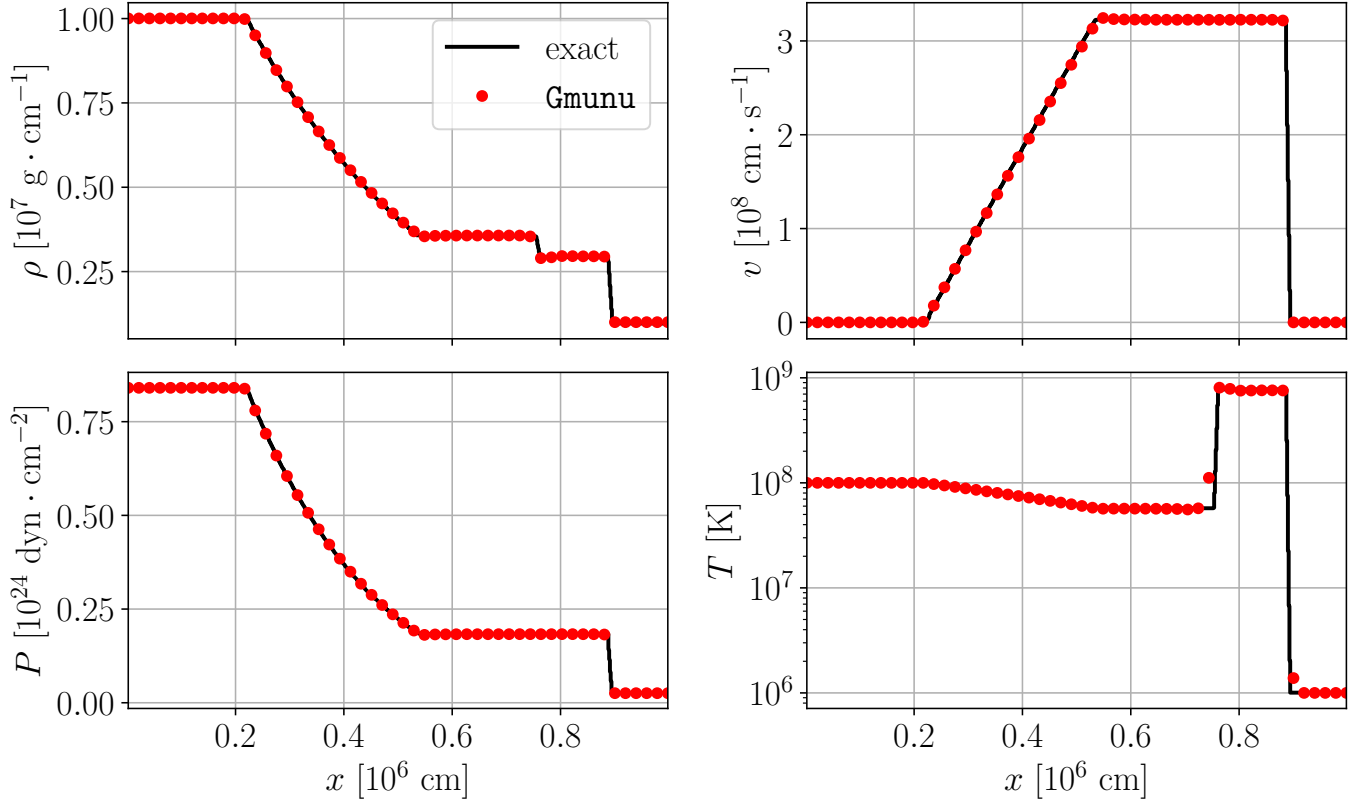


Figure 4. Profiles of rest-mass density ρ (*upper left*), velocity v (*upper right*), pressure P (*lower left*), and temperature T (*lower right*) at $t = 8 \times 10^{-4}$ s for the Newtonian real gas shock tube test 1 of Zingale & Katz (2015). Red dots: numerical results from Gmnu; black solid lines: exact reference solution. The excellent agreement validates the stellar EoS implementation.

contribute. The piecewise-parabolic method (Colella & Woodward 1984) used by Papatheodore & Messer (2014) is generally less diffusive and more accurate in smooth regions than the MC reconstruction adopted here. However, because the time-integration scheme and Riemann solvers employed in their work are not documented, a more detailed comparison with Papatheodore & Messer (2014) is not possible here. A more detailed investigation is warranted to assess how different coupling strategies (fully coupled vs. operator-split) influence post-shock burning dynamics and the formation of secondary shocks.

4. APPLICATION EXAMPLE: CCSNE IN 1D

Core-collapse supernovae (CCSNe) provide highly demanding test beds due to their multi-physics and multi-scale nature. In this section, we present spherically symmetric (1D) simulations of CCSNe with nuclear burning.

We consider the collapse of two solar-metallicity progenitors: a $9 M_{\odot}$ star (Sukhbold et al. 2016) and a $20 M_{\odot}$ star (Woosley & Heger 2007). The SFHo EoS (Steiner et al. 2013) is adopted for the NSE regime. Time integration is performed with the IMEX-SSP2(2,2,2) scheme (Pareschi & Russo 2005), and spa-

tial reconstruction uses the second-order monotonized central (MC) limiter (van Leer 1974). The computational domain extends over $r \in [0, 10^5]$ km with $N_r = 128$ and up to $l_{\max} = 13$ mesh-refinement levels, yielding a finest grid spacing of $\Delta r \approx 191$ m. Refinement criteria follow Cheong et al. (2023).

Neutrino transport is treated with the energy-dependent two-moment scheme of Cheong et al. (2023). Microphysics is provided by NuLib (O’Connor 2015), with interaction rates consistent with O’Connor et al. (2018). The energy space is discretized into 18 logarithmic groups spanning 1–280 MeV. Since NuLib requires a nuclear EoS under the assumption of NSE, neutrino interactions are included only in regions with $T > 5$ GK. While this introduces a simplification at lower temperatures, it remains a reasonable choice for the CCSN dynamics studied here. Nevertheless, a more general treatment that accounts for non-NSE effects will be pursued in future work.

Free neutrons and protons are included as advected species but do not participate in the 13-isotope α -chain reactions. Their inclusion ensures that the composition can represent an arbitrary Y_e when material cooled by neutrino processes enters the low-temperature regime

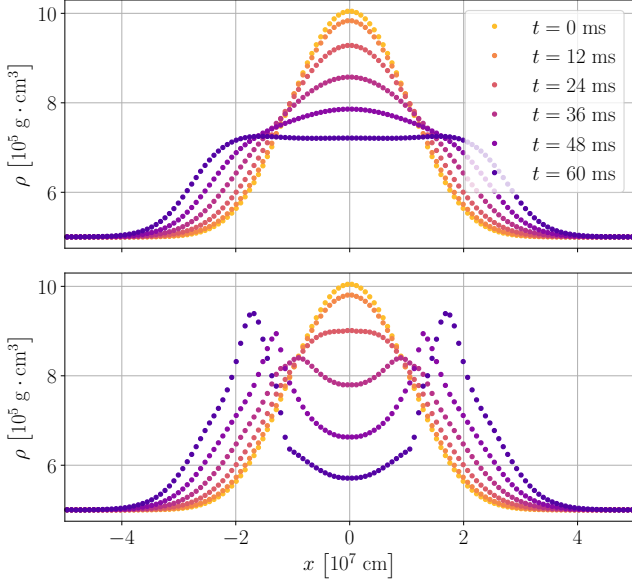


Figure 5. Snapshots of the rest-mass density ρ at six times for the Newtonian real gas acoustic pulse test (Zingale et al. 2019; Hasenour & Duffell 2025). The upper panel shows pure hydrodynamics, and the lower panel includes nuclear reactions via the 13-species network `approx13`. When nuclear burning is included, the expansion dynamics are visibly altered.

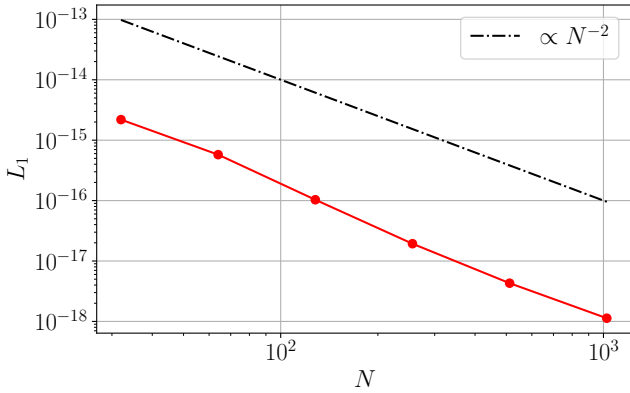


Figure 6. Volume-weighted L_1 -norm versus resolution N for the Newtonian real gas acoustic pulse at $t = 0.02 \text{ s}$. Second-order ideal scaling is shown with a dashed line, confirming that the implementation achieves the expected convergence rate.

where the network is active. It also allows the NSE solver to operate consistently within the mixed EoS region ($5 < T < 5.8 \text{ GK}$). A more complete network that explicitly includes neutrons, protons, and heavier nuclei such as ^{56}Fe would remove this limitation; extending the reaction set in this direction is planned for future work.

In the post-bounce phase of a CCSN, the gain region is the layer between the stalled accretion shock and the

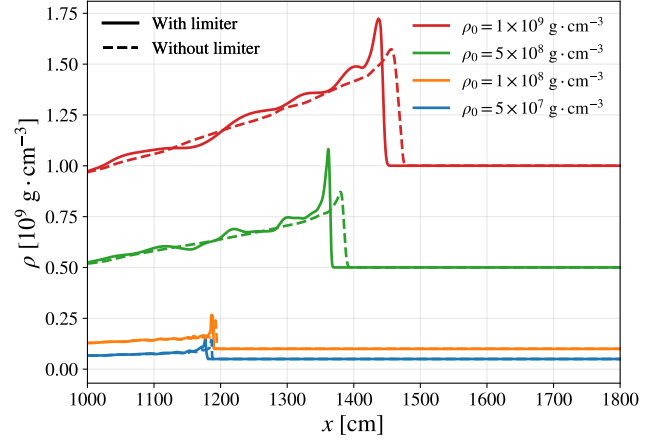


Figure 7. Rest-mass density profiles ρ at $t = 10^{-6} \text{ s}$ for different models with (solid lines) and without (dashed lines) burning suppression at shocks. We qualitatively reproduce the results of Papatheodore & Messer (2014), showing that shocks propagate faster when burning is not suppressed. Minor offsets in shock position are expected due to slight differences in the evaluation time and numerical treatment. Unlike in Papatheodore & Messer (2014), we do not observe the secondary shock feature, which may be related to the IMEX integration scheme used here.

neutrinosphere where net neutrino heating occurs. In this zone, absorption of electron-type neutrinos dominates over neutrino cooling, resulting in a positive net heating rate. Matter advected through the gain layer can acquire sufficient thermal and pressure support to aid shock revival, making it a key diagnostic for assessing the efficiency of the neutrino-driven explosion mechanism. Following this physical picture, we estimate the net neutrino heating rate by

$$\dot{Q}_\nu = \int_{\text{gain region}} \left[\int s_\nu dV_\nu \right] \sqrt{\gamma} dV, \quad (30)$$

where s_ν denotes the neutrino-matter energy coupling source term (Cheong et al. 2023), dV_ν is the volume element in energy space, and dV the spatial volume element. The gain region is defined as the region where $\rho < 3 \times 10^{10} \text{ g} \cdot \text{cm}^{-3}$, the entropy per baryon exceeds $6 k_B$, and $\int s_\nu dV_\nu > 0$.

The diagnostic explosion energy is given by

$$E_{\text{exp}} = \int_{\varepsilon_{\text{exp}} > 0, v_r > 0} \varepsilon_{\text{exp}} \sqrt{\gamma} dV, \quad (31)$$

where the energy density ε_{exp} is defined as

$$\varepsilon_{\text{exp}} = W\rho(-h_{\text{th}}u_t - 1). \quad (32)$$

Here, $u_t = W(-\alpha + \beta_i v^i)$, v_r is the radial velocity, and

$$h_{\text{th}} = 1 + (\epsilon - \epsilon_0) + \frac{P}{\rho} \quad (33)$$

is the specific enthalpy including only the thermal internal energy. In this expression, ϵ is the specific internal energy, and ϵ_0 is the corresponding zero-point obtained for the same rest-mass density and electron fraction but at zero temperature (Betranhandy & O’Connor 2020; Cheong et al. 2025). By construction, $\epsilon_{\text{exp}} > 0$ corresponds to the Bernoulli criterion for unbound material.¹ In the Newtonian limit, equation (32) reduces to the commonly used diagnostic explosion energy in Newtonian CCSN simulations, where the gravitational binding energy is encoded in u_t .

The mass accretion rate at radius r is computed as

$$\dot{M}(r) = \int_{S(r)} \rho W v^r \sqrt{\gamma} dA, \quad (34)$$

where the integral is performed over the spherical surface $S(r)$. These diagnostics are widely adopted in the CCSN community to quantify the interplay of neutrino heating, explosion energetics, and mass inflow, and thus provide a direct basis for comparing with previous studies in both Newtonian and relativistic frameworks.

Since spherically symmetric iron-core collapse supernova models usually do not explode without additional treatment, we employ enhanced neutrino heating to trigger shock revival (Blinnikov & Bartunov 1993; Woosley & Weaver 1995; Ugliano et al. 2012; Perego et al. 2015; Ertl et al. 2016; Couch et al. 2020; Boccioli et al. 2021; Gogilashvili et al. 2023). Following Gogilashvili et al. (2023), we multiply the energy–momentum and Y_e source terms from electron-type neutrinos in the gain region by a constant factor f_{heat} . While Gogilashvili et al. (2023) reported explosions of the 20 M_\odot model for $f_{\text{heat}} \leq 2.4$, here we adopt $f_{\text{heat}} = 2.8$ for all cases, consistent with Navó et al. (2023). We emphasize that this scheme is artificial and requires calibration; self-consistent explosions require multidimensional simulations. Here it is used solely to probe the role of nuclear burning behind the shock.

The initialization of composition depends on thermodynamic conditions. In high-density regions where NSE is expected, abundances are computed with the NSE solver (Section 2.3.2). In non-NSE regions, the nuclei present in the progenitor profiles may not match those in the adopted network. We therefore map progenitor abundances to the network species and rescale mass frac-

tions to enforce $\sum X_l = 1$. The network then relaxes dynamically over the first few timesteps.

We perform six simulations: for each progenitor, (i) a baseline case, (ii) a run with enhanced neutrino heating, and (iii) a run with both enhanced heating and nuclear burning.

Figure 8 summarizes the evolution of composition layers for the 9 M_\odot and 20 M_\odot progenitors under these setups. For visualization, isotopes are grouped into six categories: iron-group (^{44}Ti , ^{48}Cr , ^{52}Fe , ^{56}Ni), silicon-group (^{28}Si , ^{32}S , ^{36}Ar , ^{40}Ca), oxygen-group (^{16}O , ^{20}Ne , ^{24}Mg), alpha particle, neutron, and proton. The dominant group (maximum mass fraction) is assigned in each grid cell. Mass shells from 1 to 3 M_\odot are overplotted in increments of 0.05 M_\odot to illustrate advection and expansion. Diagnostic quantities include the shock radius, proto-neutron star (PNS) surface, and temperature thresholds of $T = 5$ GK. Note that **Gmnu** enforces NSE in the range 5–5.8 GK (see Section 2.3.2).

All baseline runs without enhanced heating or nuclear burning fail to explode. Our 20 M_\odot baseline model is consistent with previous benchmarks obtained using different codes (O’Connor et al. 2018; Ng et al. 2024; Cheong et al. 2024). The 9 M_\odot model has also been reported as non-exploding in one-dimensional simulations (Radice et al. 2017). Despite differences in microphysics and gravity treatments—Radice et al. (2017) adopted the stiffer LS220 EoS (Lattimer & Swesty 1991) and Newtonian gravity with an effective potential (Marek et al. 2006), whereas our models employ full general relativity with the SFHo EoS—our results are qualitatively consistent.

All models with enhanced neutrino heating successfully explode. Although the shock and PNS radii evolve similarly across setups, the inclusion of nuclear burning significantly alters the post-shock composition. As shown in Figure 8, when the post-shock matter cools below 5 GK, explosive Si/O burning produces additional iron-group nuclei.

Because assigning layers by dominant mass fraction is approximate, we also examine the radial velocity v_r and mean mass number \bar{A} in mass coordinates (Figure 9). For $T > 5$ GK, \bar{A} is interpolated from the SFHo EoS; otherwise, it is computed directly from mass fractions.

At early times, high post-shock temperatures dissociate heavy nuclei (Si, Fe group) into free nucleons and α particles, reducing \bar{A} . This dissociation absorbs ~ 8 MeV per nucleon, draining energy from the shock and causing it to stall. As the shock weakens, material behind it cools faster than newly shocked matter heats, and the shock temperature eventually drops below 5 GK. Without nuclear burning, compositions ef-

¹ Strictly speaking, the Bernoulli criterion is not the only possible definition of unbound matter, and can differ from more conservative approaches that account for long-term binding to the proto-neutron star. Nevertheless, it remains the standard diagnostic in CCSN studies and facilitates direct comparison across different works.

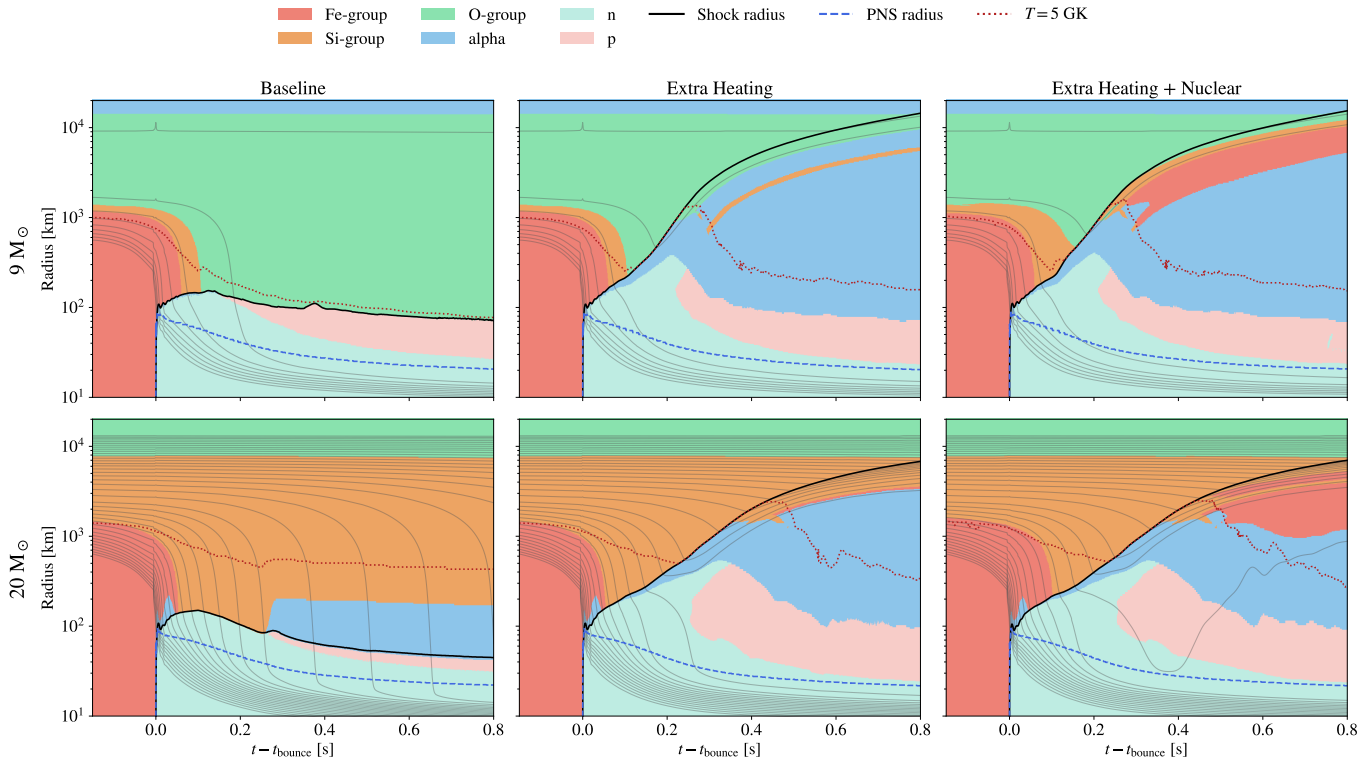


Figure 8. Temporal evolution of composition layers in the $9 M_{\odot}$ (*top*) and $20 M_{\odot}$ (*bottom*) progenitors under three setups (*left to right*): baseline, enhanced neutrino heating, and heating plus nuclear burning. Isotopes are grouped into six categories: iron-group (^{44}Ti , ^{48}Cr , ^{52}Fe , ^{56}Ni), silicon-group (^{28}Si , ^{32}S , ^{36}Ar , ^{40}Ca), oxygen-group (^{16}O , ^{20}Ne , ^{24}Mg), alpha particle, neutron, and proton. Overplotted lines mark the shock radius, PNS surface, and temperature thresholds of $T = 5$ GK. Mass shells from 1 to $3 M_{\odot}$ in increments of $0.05 M_{\odot}$ are shown. The figure highlights the role of neutrino heating and nuclear burning in modifying the post-shock composition during early post-bounce evolution.

fectively freeze at this stage. With burning included, regions with $T < 5$ GK undergo Si burning, steadily driving matter toward the iron group and increasing \bar{A} .

To further quantify the role of nuclear burning in the explosion dynamics, Figure 10 compares the time evolution of neutrino heating rate, mass accretion rate, and diagnostic explosion energy. In both cases, the onset of explosion is primarily controlled by neutrino heating, as reflected by the similar decline in heating rate and accretion rate once shock revival occurs, regardless of whether nuclear burning is included. Nevertheless, burning behind the shock contributes an additional $\sim 10\%$ to the explosion energy, amounting to $\mathcal{O}(10^{49-50})$ erg. Although subdominant compared to neutrino heating, this contribution is non-negligible: it strengthens the explosion energetics, accelerates shock expansion, and directly alters the composition of the ejecta.

These 1D CCSN simulations demonstrate that **G**munu can robustly evolve the coupled system of hydrodynamics, gravity, neutrino transport, and nuclear burning under challenging conditions. While baseline models without enhanced neutrino heating fail to explode, consistent with previous 1D results, the inclusion of an artificial

heating factor revives the shock. Incorporating nuclear burning further modifies the post-shock composition and dynamics, highlighting the role of explosive nucleosynthesis in shaping the ejecta. Together, these tests verify that the nuclear burning module integrates consistently with the microphysics and dynamical solvers, providing a foundation for future multidimensional, self-consistent CCSN studies with **G**munu. Looking ahead, these capabilities will enable detailed investigations of nucleosynthesis yields, neutrino signals, and gravitational-wave signatures from core-collapse supernovae in more realistic multidimensional settings.

5. CONCLUSIONS

We have presented the implementation of nuclear reaction networks in the general-relativistic radiation hydrodynamics code **G**munu. The new module has been verified through a suite of benchmark problems, including conserved-to-primitive tests with a stellar equation of state, one-zone silicon burning, and Newtonian shock-tube, acoustic pulse tests and detonation fronts of Type Ia supernovae. These results confirm that the coupling between the nuclear network, the equation of state, and

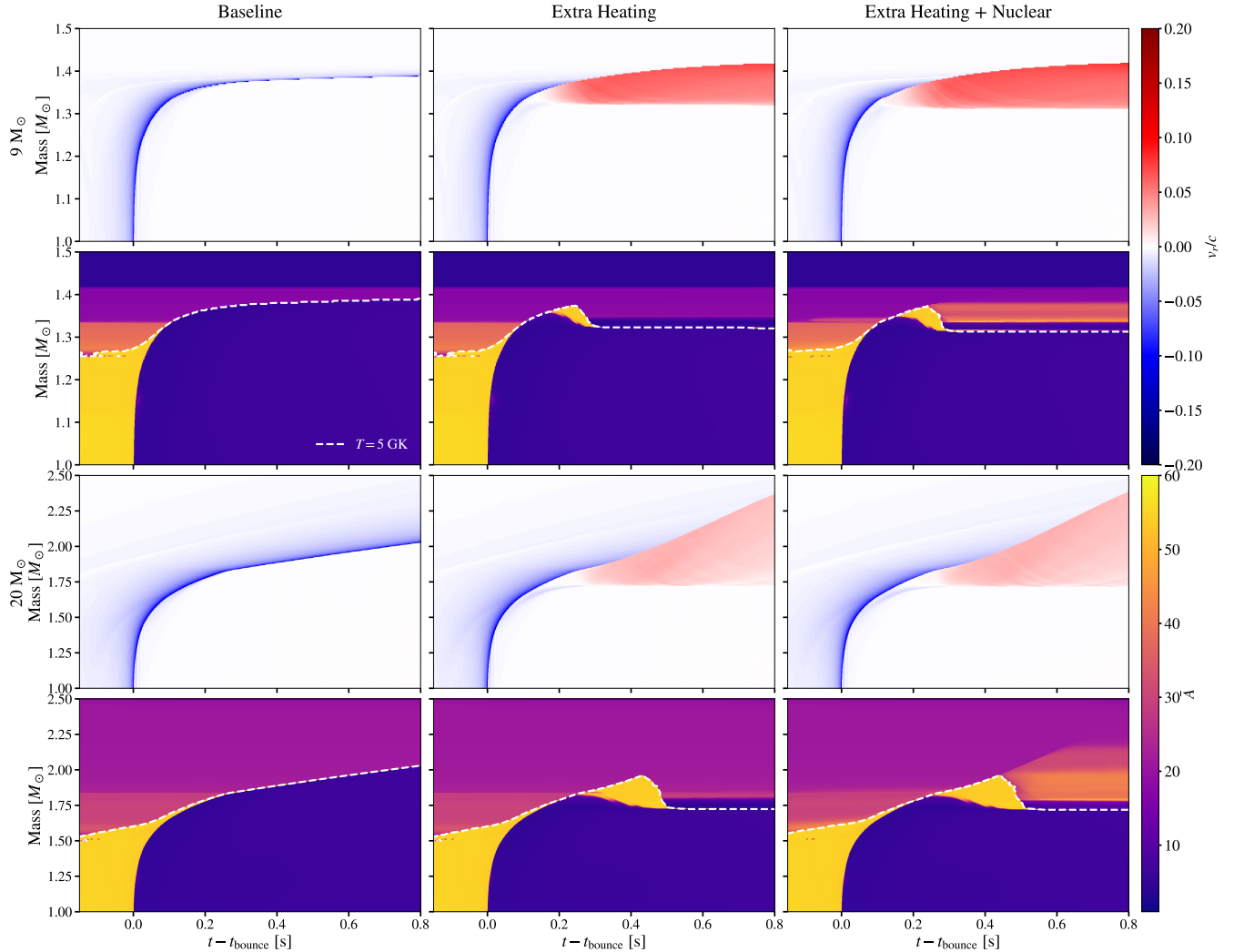


Figure 9. Time evolution of radial velocity v_r (odd rows) and mean mass number \bar{A} (even rows) in CCSN simulations of $9 M_{\odot}$ (top) and $20 M_{\odot}$ (bottom) progenitors. Columns correspond to baseline (left), enhanced heating (middle), and heating plus burning (right). In baseline runs, the shock is not revived and composition remains largely unchanged. Enhanced heating prolongs shock expansion, but the post-shock matter is dominated by light nuclei. With nuclear burning, \bar{A} increases after a few 100 ms post-bounce as explosive burning drives material toward heavier nuclei. The comparison shows that lower-mass progenitors undergo earlier composition changes, while higher-mass models require both heating and burning for significant enrichment.

the hydrodynamics solver is robust, conserving both the electron fraction and the total mass fraction to machine precision.

We further demonstrated the application of this framework to one-dimensional core-collapse supernova simulations. The results reproduce the expected non-exploding behavior of baseline 1D models and confirm that artificially enhanced neutrino heating can trigger shock revival. When nuclear burning is included, the post-shock composition evolves dynamically, with silicon and oxygen layers progressively converted to iron-group nuclei as the shock expands and cools. This high-

lights the role of explosive burning in shaping ejecta composition and demonstrates that reduced nuclear networks can be stably integrated in fully coupled, general-relativistic, radiation-hydrodynamic simulations.

Importantly, to the best of our knowledge, **Gmnu** is the first code that combines general relativity, M1 neutrino transport, magnetohydrodynamics, and in-situ nuclear burning within a single framework. Although the current networks are limited in size, they provide a valuable bridge between simplified hydrodynamic models and large-scale post-processing calculations, offering

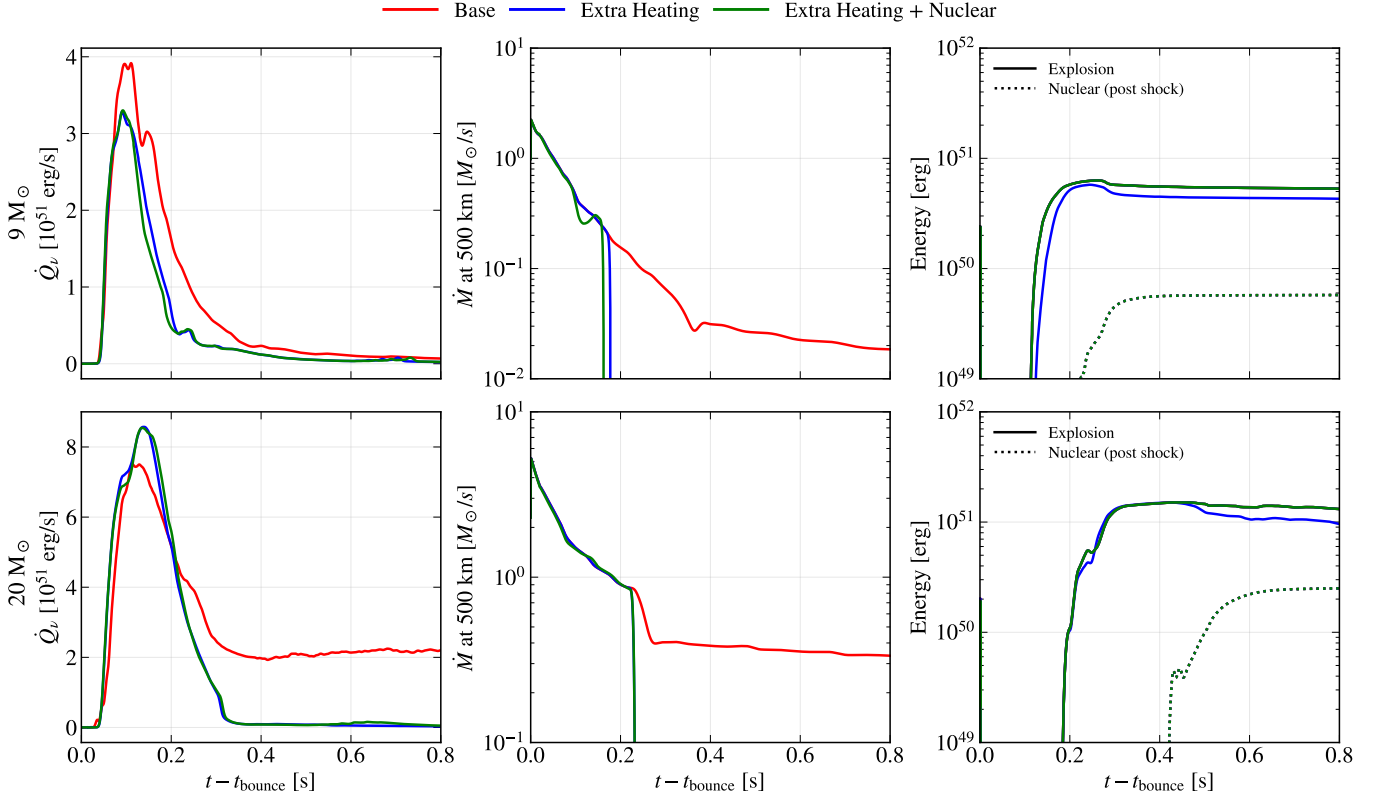


Figure 10. Time evolution of the net neutrino heating rate in the gain region (*left*), mass accretion rate at 500 km (*middle*), and diagnostic explosion energy (*right*) in core-collapse supernova simulations of $9 M_{\odot}$ (*top*) and $20 M_{\odot}$ (*bottom*) progenitors. In the exploding models, both the net neutrino heating rate and the mass accretion rate decrease significantly once shock revival is achieved. These quantities exhibit similar behavior with and without nuclear burning, indicating that neutrino heating dominates the early explosion dynamics. However, nuclear burning in the post-shock region contributes an additional $\mathcal{O}(10^{49-50})$ erg (dotted lines), corresponding to about $\mathcal{O}(10)$ % of the explosion energy. This contribution enhances the final explosion energy and leads to faster shock expansion (not shown).

more realistic composition and thermal profiles to seed follow-up nucleosynthesis studies.

Looking ahead, this work establishes a robust foundation for exploring a wide range of astrophysical explosion scenarios. Future developments will focus on: (i) multi-dimensional CCSN simulations with self-consistent neutrino heating to capture convection, turbulence, and asphericity; (ii) adaptive nuclear networks that expand dynamically depending on local conditions, eventually incorporating up-to-date libraries such as REACLIB and `pynucastro` (Willcox & Zingale 2018; Smith et al. 2023; `pynucastro` development team et al. 2025); (iii) systematic studies of nucleosynthesis yields across progenitor models; and (iv) connections to multi-messenger observables, including neutrinos, gravitational waves, and electromagnetic transients. Beyond core-collapse supernovae, the framework is also directly applicable to other explosive phenomena where nuclear burning plays a central role, such as collapsars, white dwarf–neutron star mergers, and white dwarf–white dwarf mergers.

Together, these advances will allow `Gmnu` to become a comprehensive platform for probing the interplay of gravity, neutrino transport, magnetism, and nuclear burning in some of the universe’s most energetic events.

We thank Albino Perego and David Radice for valuable discussions on bridging NSE and non-NSE equations of state. We are also grateful to Gerard Navó and Martin Obergaulinger for their insights regarding the initial setup of the core-collapse supernova tests. We further thank Peter Siu Hei Cheung for helpful general discussions. P.C.-K.C. acknowledges support from the National Science Foundation (NSF) under Grant PHY-2020275, awarded to the Network for Neutrinos, Nuclear Astrophysics, and Symmetries (N3AS).

The simulations in this work have been performed on the third UNH supercomputer Marvin, also known as Plasma, which is supported by NSF/Major Research Instrumentation (MRI) program under grant number AGS-1919310. The simulations have also been performed on the Expanse cluster at San Diego Supercomputer Centre through allocation PHY230104 and PHY230129 from the Advanced Cyberinfrastructure Coordination Ecosystem: Services & Support (ACCESS) program (Boerner et al. 2023), which is supported by National Science Foundation grants #2138259, #2138286, #2138307, #2137603, and #2138296.

Software: The results of this work were produced by utilising `Gmunu` (Cheong et al. 2020, 2021) and the energy-dependent M1 neutrino transport module (Cheong et al. 2023). The tabulated neutrino interaction were provided with `NuLib` (O’Connor 2015). The EoS in the non-NSE region is provided with `helmeos` (Timmes & Swesty 2000). The nuclear networks used in this work (i.e. the `aprox13`) (Timmes 1999; Timmes et al. 2000) are publicly available at <https://cococubed.com/>. The data of the simulations were post-processed and visualised with `yt` (Turk et al. 2011), `NumPy` (Harris et al. 2020), `pandas` (pandas development team 2020; Wes McKinney 2010), `SciPy` (Virtanen et al. 2020) and `Matplotlib` (Hunter 2007; Caswell et al. 2023).

REFERENCES

- Abbott, B. P., Abbott, R., Abbott, T. D., et al. 2017, *PhRvL*, 119, 161101, doi: [10.1103/PhysRevLett.119.161101](https://doi.org/10.1103/PhysRevLett.119.161101)
- Ascher, U. M., Ruuth, S. J., & Spiteri, R. J. 1997, *Applied Numerical Mathematics*, 25, 151, doi: [https://doi.org/10.1016/S0168-9274\(97\)00056-1](https://doi.org/10.1016/S0168-9274(97)00056-1)
- Baumgarte, T. W., & Shapiro, S. L. 2020, *PhRvD*, 102, 104001, doi: [10.1103/PhysRevD.102.104001](https://doi.org/10.1103/PhysRevD.102.104001)
- Betranhandy, A., & O’Connor, E. 2020, *PhRvD*, 102, 123015, doi: [10.1103/PhysRevD.102.123015](https://doi.org/10.1103/PhysRevD.102.123015)
- Blinnikov, S. I., & Bartunov, O. S. 1993, *A&A*, 273, 106
- Boccioli, L., Mathews, G. J., & O’Connor, E. P. 2021, *ApJ*, 912, 29, doi: [10.3847/1538-4357/abe767](https://doi.org/10.3847/1538-4357/abe767)
- Boerner, T. J., Deems, S., Furlani, T. R., Knuth, S. L., & Towns, J. 2023, in *Practice and Experience in Advanced Research Computing, PEARC ’23* (New York, NY, USA: Association for Computing Machinery), 173–176, doi: [10.1145/3569951.3597559](https://doi.org/10.1145/3569951.3597559)

- Brady, R., & Zingale, M. 2025, *Research Notes of the American Astronomical Society*, 9, 113, doi: [10.3847/2515-5172/add686](https://doi.org/10.3847/2515-5172/add686)
- Bruenn, S. W., Lentz, E. J., Hix, W. R., et al. 2016, *ApJ*, 818, 123, doi: [10.3847/0004-637X/818/2/123](https://doi.org/10.3847/0004-637X/818/2/123)
- Bruenn, S. W., Blondin, J. M., Hix, W. R., et al. 2020, *ApJS*, 248, 11, doi: [10.3847/1538-4365/ab7aff](https://doi.org/10.3847/1538-4365/ab7aff)
- Buras, R., Rampp, M., Janka, H. T., & Kifonidis, K. 2006, *A&A*, 447, 1049, doi: [10.1051/0004-6361:20053783](https://doi.org/10.1051/0004-6361:20053783)
- Calder, A. C., Townsley, D. M., Seitenzahl, I. R., et al. 2007, *ApJ*, 656, 313, doi: [10.1086/510709](https://doi.org/10.1086/510709)
- Caswell, T. A., Lee, A., de Andrade, E. S., et al. 2023, *matplotlib/matplotlib: REL: v3.7.1, v3.7.1*, Zenodo, doi: [10.5281/zenodo.7697899](https://doi.org/10.5281/zenodo.7697899)
- Cavaglieri, D., & Bewley, T. 2015, *Journal of Computational Physics*, 286, 172, doi: [10.1016/j.jcp.2015.01.031](https://doi.org/10.1016/j.jcp.2015.01.031)
- Chabrier, G., & Potekhin, A. Y. 1998, *PhRvE*, 58, 4941, doi: [10.1103/PhysRevE.58.4941](https://doi.org/10.1103/PhysRevE.58.4941)
- Cheong, P. C.-K., Foucart, F., Duez, M. D., et al. 2024, *ApJ*, 975, 116, doi: [10.3847/1538-4357/ad7825](https://doi.org/10.3847/1538-4357/ad7825)
- Cheong, P. C.-K., Lam, A. T.-L., Ng, H. H.-Y., & Li, T. G. F. 2021, *MNRAS*, 508, 2279, doi: [10.1093/mnras/stab2606](https://doi.org/10.1093/mnras/stab2606)
- Cheong, P. C.-K., Lin, L.-M., & Li, T. G. F. 2020, *Classical and Quantum Gravity*, 37, 145015, doi: [10.1088/1361-6382/ab8e9c](https://doi.org/10.1088/1361-6382/ab8e9c)
- Cheong, P. C.-K., Ng, H. H.-Y., Lam, A. T.-L., & Li, T. G. F. 2023, *ApJS*, 267, 38, doi: [10.3847/1538-4365/acd931](https://doi.org/10.3847/1538-4365/acd931)
- Cheong, P. C.-K., Pitik, T., Longo Micchi, L. F., & Radice, D. 2025, *ApJL*, 978, L38, doi: [10.3847/2041-8213/ada1cc](https://doi.org/10.3847/2041-8213/ada1cc)
- Cheong, P. C.-K., Pong, D. Y. T., Yip, A. K. L., & Li, T. G. F. 2022, *ApJS*, 261, 22, doi: [10.3847/1538-4365/ac6ccc](https://doi.org/10.3847/1538-4365/ac6ccc)
- Colella, P., & Woodward, P. R. 1984, *Journal of Computational Physics*, 54, 174, doi: [10.1016/0021-9991\(84\)90143-8](https://doi.org/10.1016/0021-9991(84)90143-8)
- Couch, S. M., Chatzopoulos, E., Arnett, W. D., & Timmes, F. X. 2015, *ApJL*, 808, L21, doi: [10.1088/2041-8205/808/1/L21](https://doi.org/10.1088/2041-8205/808/1/L21)
- Couch, S. M., Warren, M. L., & O'Connor, E. P. 2020, *ApJ*, 890, 127, doi: [10.3847/1538-4357/ab609e](https://doi.org/10.3847/1538-4357/ab609e)
- Ertl, T., Janka, H. T., Woosley, S. E., Sukhbold, T., & Ugliano, M. 2016, *ApJ*, 818, 124, doi: [10.3847/0004-637X/818/2/124](https://doi.org/10.3847/0004-637X/818/2/124)
- Fryxell, B., Müller, E., & Arnett, D. 1989, *Hydrodynamics and nuclear burning*, Max-Planck-Institut für Physik und Astrophysik München: MPA (Max-Planck-Inst. für Physik und Astrophysik). <https://books.google.com/books?id=4LQhtwAACAAJ>
- Fujibayashi, S., Jockel, C., Kawaguchi, K., Sekiguchi, Y., & Shibata, M. 2025, *ApJ*, 981, 119, doi: [10.3847/1538-4357/adb0b8](https://doi.org/10.3847/1538-4357/adb0b8)
- Gogilashvili, M., Murphy, J. W., & O'Connor, E. P. 2023, *MNRAS*, 524, 4109, doi: [10.1093/mnras/stad2155](https://doi.org/10.1093/mnras/stad2155)
- Gronow, S., Collins, C., Ohlmann, S. T., et al. 2020, *A&A*, 635, A169, doi: [10.1051/0004-6361/201936494](https://doi.org/10.1051/0004-6361/201936494)
- Harris, C. R., Millman, K. J., van der Walt, S. J., et al. 2020, *Nature*, 585, 357, doi: [10.1038/s41586-020-2649-2](https://doi.org/10.1038/s41586-020-2649-2)
- Harris, J. A., Hix, W. R., Chertkow, M. A., et al. 2017, *ApJ*, 843, 2, doi: [10.3847/1538-4357/aa76de](https://doi.org/10.3847/1538-4357/aa76de)
- Hasenour, D. L., & Duffell, P. C. 2025, *ApJ*, 981, 63, doi: [10.3847/1538-4357/adaeb0](https://doi.org/10.3847/1538-4357/adaeb0)
- Hix, W. R., & Thielemann, F.-K. 1996, *ApJ*, 460, 869, doi: [10.1086/177016](https://doi.org/10.1086/177016)
- Hix, W. R., & Thielemann, F. K. 1999, *Journal of Computational and Applied Mathematics*, 109, 321, doi: [10.48550/arXiv.astro-ph/9906478](https://doi.org/10.48550/arXiv.astro-ph/9906478)
- Hunter, J. D. 2007, *Computing in Science and Engineering*, 9, 90, doi: [10.1109/MCSE.2007.55](https://doi.org/10.1109/MCSE.2007.55)
- Kastaun, W., Kalinani, J. V., & Ciolfi, R. 2021, *PhRvD*, 103, 023018, doi: [10.1103/PhysRevD.103.023018](https://doi.org/10.1103/PhysRevD.103.023018)
- Lattimer, J. M., & Swesty, D. F. 1991, *NuPhA*, 535, 331, doi: [10.1016/0375-9474\(91\)90452-C](https://doi.org/10.1016/0375-9474(91)90452-C)
- Leung, S. C., Chu, M. C., & Lin, L. M. 2015, *MNRAS*, 454, 1238, doi: [10.1093/mnras/stv1923](https://doi.org/10.1093/mnras/stv1923)
- Lippuner, J., & Roberts, L. F. 2017, *ApJS*, 233, 18, doi: [10.3847/1538-4365/aa94cb](https://doi.org/10.3847/1538-4365/aa94cb)
- Marek, A., Dimmelmeier, H., Janka, H. T., Müller, E., & Buras, R. 2006, *A&A*, 445, 273, doi: [10.1051/0004-6361:20052840](https://doi.org/10.1051/0004-6361:20052840)
- Mewes, V., Zlochower, Y., Campanelli, M., et al. 2020, *PhRvD*, 101, 104007, doi: [10.1103/PhysRevD.101.104007](https://doi.org/10.1103/PhysRevD.101.104007)
- Montero, P. J., Baumgarte, T. W., & Müller, E. 2014, *PhRvD*, 89, 084043, doi: [10.1103/PhysRevD.89.084043](https://doi.org/10.1103/PhysRevD.89.084043)
- Montero, P. J., Janka, H.-T., & Müller, E. 2012, *ApJ*, 749, 37, doi: [10.1088/0004-637X/749/1/37](https://doi.org/10.1088/0004-637X/749/1/37)
- Mueller, E. 1986, *A&A*, 162, 103
- Nakamura, K., Takiwaki, T., Kotake, K., & Nishimura, N. 2014, *ApJ*, 782, 91, doi: [10.1088/0004-637X/782/2/91](https://doi.org/10.1088/0004-637X/782/2/91)
- Navó, G., Reichert, M., Obergaulinger, M., & Arcones, A. 2023, *ApJ*, 951, 112, doi: [10.3847/1538-4357/acd640](https://doi.org/10.3847/1538-4357/acd640)
- Ng, H. H.-Y., Cheong, P. C.-K., Lam, A. T.-L., & Li, T. G. F. 2024, *ApJS*, 272, 9, doi: [10.3847/1538-4365/ad2fbd](https://doi.org/10.3847/1538-4365/ad2fbd)
- O'Connor, E. 2015, *ApJS*, 219, 24, doi: [10.1088/0067-0049/219/2/24](https://doi.org/10.1088/0067-0049/219/2/24)
- O'Connor, E., & Ott, C. D. 2010, *Classical and Quantum Gravity*, 27, 114103, doi: [10.1088/0264-9381/27/11/114103](https://doi.org/10.1088/0264-9381/27/11/114103)

- O'Connor, E., Bollig, R., Burrows, A., et al. 2018, *Journal of Physics G Nuclear Physics*, 45, 104001, doi: [10.1088/1361-6471/aadeae](https://doi.org/10.1088/1361-6471/aadeae)
- pandas development team, T. 2020, pandas-dev/pandas: Pandas, latest, Zenodo, doi: [10.5281/zenodo.3509134](https://doi.org/10.5281/zenodo.3509134)
- Papatheodore, T. L., & Messer, O. E. B. 2014, *ApJ*, 782, 12, doi: [10.1088/0004-637X/782/1/12](https://doi.org/10.1088/0004-637X/782/1/12)
- Pareschi, L., & Russo, G. 2005, *Journal of Scientific computing*, 25, 129
- Perego, A., Hempel, M., Fröhlich, C., et al. 2015, *ApJ*, 806, 275, doi: [10.1088/0004-637X/806/2/275](https://doi.org/10.1088/0004-637X/806/2/275)
- Press, W. H., Teukolsky, S. A., Vetterling, W. T., & Flannery, B. P. 1996, *Numerical recipes in Fortran 90*, Vol. 2 (Cambridge university press Cambridge)
- pynucastro development team, Boyd, B., Cao, L., et al. 2025, pynucastro/pynucastro: pynucastro 2.8.0, 2.8.0, Zenodo, doi: [10.5281/zenodo.17455462](https://doi.org/10.5281/zenodo.17455462)
- Radice, D., Burrows, A., Vartanyan, D., Skinner, M. A., & Dolence, J. C. 2017, *ApJ*, 850, 43, doi: [10.3847/1538-4357/aa92c5](https://doi.org/10.3847/1538-4357/aa92c5)
- Rampp, M., & Janka, H. T. 2002, *A&A*, 396, 361, doi: [10.1051/0004-6361:20021398](https://doi.org/10.1051/0004-6361:20021398)
- Rauscher, T., & Thielemann, F.-K. 2000, *Atomic Data and Nuclear Data Tables*, 75, 1, doi: [10.1006/adnd.2000.0834](https://doi.org/10.1006/adnd.2000.0834)
- Reichert, M., Winteler, C., Korobkin, O., et al. 2023, *ApJS*, 268, 66, doi: [10.3847/1538-4365/acf033](https://doi.org/10.3847/1538-4365/acf033)
- Sandoval, M. A., Hix, W. R., Messer, O. E. B., Lentz, E. J., & Harris, J. A. 2021, *ApJ*, 921, 113, doi: [10.3847/1538-4357/ac1d49](https://doi.org/10.3847/1538-4357/ac1d49)
- Seitenzahl, I. R., Timmes, F. X., Marin-Laffèche, A., et al. 2008, *ApJL*, 685, L129, doi: [10.1086/592501](https://doi.org/10.1086/592501)
- Seitenzahl, I. R., Townsley, D. M., Peng, F., & Truran, J. W. 2009, *Atomic Data and Nuclear Data Tables*, 95, 96, doi: [10.1016/j.adt.2008.08.001](https://doi.org/10.1016/j.adt.2008.08.001)
- Siegel, D. M., Mösta, P., Desai, D., & Wu, S. 2018, *ApJ*, 859, 71, doi: [10.3847/1538-4357/aabcc5](https://doi.org/10.3847/1538-4357/aabcc5)
- Smith, A. I., Johnson, E. T., Chen, Z., et al. 2023, *The Astrophysical Journal*, 947, 65, doi: [10.3847/1538-4357/acbaff](https://doi.org/10.3847/1538-4357/acbaff)
- Steiner, A. W., Hempel, M., & Fischer, T. 2013, *ApJ*, 774, 17, doi: [10.1088/0004-637X/774/1/17](https://doi.org/10.1088/0004-637X/774/1/17)
- Strang, G. 1968, *SIAM Journal on Numerical Analysis*, 5, 506, doi: [10.1137/0705041](https://doi.org/10.1137/0705041)
- Sukhbold, T., Ertl, T., Woosley, S. E., Brown, J. M., & Janka, H. T. 2016, *ApJ*, 821, 38, doi: [10.3847/0004-637X/821/1/38](https://doi.org/10.3847/0004-637X/821/1/38)
- Timmes, F. X. 1999, *ApJS*, 124, 241, doi: [10.1086/313257](https://doi.org/10.1086/313257)
- Timmes, F. X., Hoffman, R. D., & Woosley, S. E. 2000, *ApJS*, 129, 377, doi: [10.1086/313407](https://doi.org/10.1086/313407)
- Timmes, F. X., & Swesty, F. D. 2000, *ApJS*, 126, 501, doi: [10.1086/313304](https://doi.org/10.1086/313304)
- Turk, M. J., Smith, B. D., Oishi, J. S., et al. 2011, *The Astrophysical Journal Supplement Series*, 192, 9, doi: [10.1088/0067-0049/192/1/9](https://doi.org/10.1088/0067-0049/192/1/9)
- Uchida, H., Shibata, M., Takahashi, K., & Yoshida, T. 2019, *ApJ*, 870, 98, doi: [10.3847/1538-4357/aaf39e](https://doi.org/10.3847/1538-4357/aaf39e)
- Uchida, H., Shibata, M., Yoshida, T., Sekiguchi, Y., & Umeda, H. 2017, *PhRvD*, 96, 083016, doi: [10.1103/PhysRevD.96.083016](https://doi.org/10.1103/PhysRevD.96.083016)
- Ugliano, M., Janka, H.-T., Marek, A., & Arcones, A. 2012, *ApJ*, 757, 69, doi: [10.1088/0004-637X/757/1/69](https://doi.org/10.1088/0004-637X/757/1/69)
- van Leer, B. 1974, *Journal of Computational Physics*, 14, 361, doi: [10.1016/0021-9991\(74\)90019-9](https://doi.org/10.1016/0021-9991(74)90019-9)
- Virtanen, P., Gommers, R., Oliphant, T. E., et al. 2020, *Nature Methods*, 17, 261, doi: [10.1038/s41592-019-0686-2](https://doi.org/10.1038/s41592-019-0686-2)
- Wallace, R. K., Woosley, S. E., & Weaver, T. A. 1982, *ApJ*, 258, 696, doi: [10.1086/160119](https://doi.org/10.1086/160119)
- Wes McKinney. 2010, in *Proceedings of the 9th Python in Science Conference*, ed. Stéfan van der Walt & Jarrod Millman, 56 – 61, doi: [10.25080/Majora-92bf1922-00a](https://doi.org/10.25080/Majora-92bf1922-00a)
- Willcox, D. E., & Zingale, M. 2018, *Journal of Open Source Software*, 3, 588, doi: [10.21105/joss.00588](https://doi.org/10.21105/joss.00588)
- Wongwathanarat, A., Janka, H.-T., Müller, E., Pllumbi, E., & Wanajo, S. 2017, *ApJ*, 842, 13, doi: [10.3847/1538-4357/aa72de](https://doi.org/10.3847/1538-4357/aa72de)
- Woosley, S. E., Arnett, W. D., & Clayton, D. D. 1973, *ApJS*, 26, 231, doi: [10.1086/190282](https://doi.org/10.1086/190282)
- Woosley, S. E., & Heger, A. 2007, *PhR*, 442, 269, doi: [10.1016/j.physrep.2007.02.009](https://doi.org/10.1016/j.physrep.2007.02.009)
- Woosley, S. E., & Weaver, T. A. 1995, *ApJS*, 101, 181, doi: [10.1086/192237](https://doi.org/10.1086/192237)
- Zingale, M., Chen, Z., Rasmussen, M., et al. 2024, *ApJ*, 966, 150, doi: [10.3847/1538-4357/ad3441](https://doi.org/10.3847/1538-4357/ad3441)
- Zingale, M., & Katz, M. P. 2015, *ApJS*, 216, 31, doi: [10.1088/0067-0049/216/2/31](https://doi.org/10.1088/0067-0049/216/2/31)
- Zingale, M., Katz, M. P., Bell, J. B., et al. 2019, *ApJ*, 886, 105, doi: [10.3847/1538-4357/ab4e1d](https://doi.org/10.3847/1538-4357/ab4e1d)